RESEARCH ARTICLE

Research on the mechanism of the two-dimensional ultrasonic surface burnishing process to enhance the wear resistance for aluminum alloy

Zhen-Yu ZHOU[1,2], **Qiu-Yang ZHENG**[1,2], **Yu LI**[1,2], **Cong DING**[1,2], **Guang-Jian PENG**[1,2,*], **Zhong-Yu PIAO**[1,2,*]

[1] *College of Mechanical Engineering, Zhejiang University of Technology, Hangzhou 310023, China*

[2] *Key Laboratory of Special Purpose Equipment and Advanced Processing Technology, Ministry of Education and Zhejiang Province, Zhejiang University of Technology, Hangzhou 310014, China*

Abstract: The gradient nanostructure is machined on the aluminum (Al) alloy by the two-dimensional ultrasonic surface burnishing process (2D-USBP). The mechanism of why the gradient nanostructure enhances wear resistance is investigated. The mechanical properties and microstructure characterization for the gradient nanostructure are performed by operating a nanoindenter, transmission electron microscopy (TEM), and electron backscattered diffraction (EBSD). Dry wear tests are performed on the samples before and after machining to evaluate the wear resistance and mechanisms. The effect of the gradient nanostructure on the wear resistance is explored by developing the crystal plasticity (CP) finite element and molecular dynamics (MD) models. The characterization results show that the 2D-USBP sample prepared a gradient structure of ~600 µm thick on the aluminum surface, increasing the surface hardness from 1.13 to 1.71 GPa and reducing the elastic modulus from 78.84 to 70.14 GPa. The optimization of the surface microstructure and the increase of the mechanical properties effectively enhance the wear resistance of the sample, with 41.20%, 39.07%, and 54.58% of the wear scar areas for the 2D-USBP treated samples to the original samples under 5, 10, and 15 N loads, respectively. The gradient nanostructure hinders the slip of dislocations inside the sample during the wear process and reduces the size and scope of plastic deformation; meanwhile, the resistance to deformation, adhesion, and crack initiation and propagation of the sample surface is improved, resulting in enhanced wear resistance.

Keywords: structural superlubricity; lattice registry; elastic deformation; strained solitons; crystal plasticity; molecular dynamics simulations

1 Introduction

Seven series of aluminum (Al) alloys with many advantages, such as high processability, high specific strength, excellent welding performance, and low density, are widely used in vehicles, buildings, bridges, and tunnels [1, 2]. Wear is the common and multiple failure types in mechanical equipment, with considerable complexity and sensitivity [3–5]. The surface of the aluminum alloy is prone to wear, and the industrial application range is limited [6]. The gradient nanostructure machined by the surface burnishing process (SBP) is considered a structure with high wear resistance [7–11].

The effect of the SBP on the wear resistance for various materials, such as forging materials, powder metallurgy materials, and coating materials, has been extensively studied. Ren et al. [12] introduced ultrasonic vibration assistance in the SBP, followed by a comparative study of the ultrasonic surface

---

* Corresponding authors: Guang-Jian PENG, E-mail: penggj@zjut.edu.cn; Zhong-Yu PIAO, E-mail: piaozy@zjut.edu.cn

burnishing process (USBP) on the wear resistance of the $Ti_5Al_4Mo_6V_2Nb_1Fe$. The wear test results showed that the USBP changed the wear mechanism of the original samples from abrasive wear to adhesion, crater, and gully with the increasing loading force. The high-hardness surface produced by machining forces the crack initiation site closer to the surface during wear, and the residual compressive stress inhibits the rate of crack expansion, considered as the main reason for the enhanced wear resistance. Liu et al. [13, 14] employed SBP on the Fe–2Cu–0.6C powder metallurgical material to produce simultaneous fine crystallization and densification of the surface layer, obtaining a high-quality surface layer with a surface hardness of 330 HV0.01 and a depth of 335 μm in the densification layer. The rolling wear test showed that SBP changes the wear mechanism, in which the crack initiation position in the machined sample is closer to the surface, and the crack length is shorter, reducing the wear amount by 50%. Ma et al. [15] performed the USBP to enhance the wear resistance of NiTi coatings prepared by laser cladding, reducing the wear volume from 92,137 $μm^3$ in the original sample to 64,011 $μm^3$. The USBP smoothes the NiTi coating surface, makes the release of nickel ions from the cladding layer less likely, and reduces the porosity inside the coating by 90%, which was responsible for the improved wear resistance.

In summary, high hardness, residual compressive stress, and smooth surface are prepared on the material surface by the SBP, considered as the main reason for improving the wear resistance. A traditional wear theory underscores that hardness predominantly determines wear resistance. Nevertheless, the plowing action during wear is an intense cold-work-hardening process for the metals, resulting in the worn surface being much harder than the original one. The wear resistance of metals depends to a certain extent on the properties of the material in the maximum hardened state, so the high hardness machined by the SBP does not contribute significantly to the wear

resistance as expected. In addition, polymer materials have lower elastic modulus, higher unloading/loading work (W_e), and lower hardness, exhibiting excellent antiwear properties. However, few studies have been devoted to investigating the effects of variation in the elastic modulus and W_e of the gradient nanostructure on the wear resistance, and the effect of high-density grain boundaries on the wear properties needs to be further studied.

The present study performed the two-dimensional ultrasonic surface burnishing process (2D-USBP) on the aluminum alloy surface to enhance the wear resistance. The mechanical properties and microstructures of gradient nanostructures machined by 2D-USBP were characterized by operating a nanoindenter, transmission electron microscopy (TEM), and electron backscattered diffraction (EBSD). Establishing crystal plasticity (CP) models and molecular dynamics (MD) models in wear processes reveal how gradient nanostructures improve the wear resistance.

2　Test and simulation

2.1　Materials and machining equipment

The experimental sample, a rectangular plate of 30 mm × 50 mm × 10 mm, was the aluminum alloy (0.1 wt% Si, 0.26 wt% Fe, 1.57 wt% Cu, 5.59 wt% Zn, 0.02 wt% Ti, 0.13 wt% Mn, 2.67 wt% Mg, 0.20 wt% Cr, and balanced Al). The 2D-USBP was used for machining the samples to introduce a gradient nanostructure and reduce the surface roughness. The detailed description of the machining, such as the advantages of the 2D ultrasonic vibration and the decision of optimized machining parameters, can be found in Refs. [16, 17]. The machining parameters used in this paper are listed in Table 1.

2.2　Characterization

The microstructures of the 2D-USBP treated samples were characterized by the EBSD and TEM. The EBSD

Table 1　2D-USBP process parameters.

Penetration depth (μm)	Spindle speed (r/min)	Feed rate (mm/min)	Ultrasonic amplitude (μm)	Ultrasonic frequency (kHz)	Lubrication method	Machining pass
150	3,000	50	9	20	10# lubricating oil	2

results were obtained via a scanning electron microscopy (SEM; MIRA 3, TESCAN) equipped with an EBSD system (C-Nano, OXFORD) at a voltage of 20 kV, tilt angle of 70°, and scan step of 0.9 μm, and analyzed by Channel and MTEX [18] software. The grain size on the surface of the 2D-USBP treated sample reaches the nanometer level and cannot be characterized by the EBSD. The ultra-thin sample for characterization was prepared using a focused ion beam on the top layer of the cross-section of the 2D-USBP treated sample, whose microstructure was observed by the TEM. The TEM picture was obtained via a TEM (Tecnai G2 S-TWIN F20, FEI) with an accelerating voltage of 200 kV.

The mechanical properties of the 2D-USBP treated samples were characterized by a nanoindenter (Technologies G200, Agilent) using a Berkovich indenter. The Berkovich indenter was loaded to 1,000 nm at a constant loading rate of 0.05 s⁻¹ under continuous stiffness measurements and held for 10 s to correct the effects of the creep. Then, the Berkovich indenter was unloaded to 10% of the maximum load and held for 100 s to determine the thermal drift rate for depth data correction. Finally, the Berkovich indenter was unloaded to zero. The position distribution of the indentation points is shown in Fig. 1.

2.3   Dry wear tests

The wear tests were performed on a tribometer (UMT-3, Bruker) based on the ball-on-disc method at a room temperature of 18–25 °C. The counterpart in the wear tests was a zirconia ceramic ball (94.5% ZrO_2 + 5.2% Y_2O_3) with a diameter of 4 mm, hardness
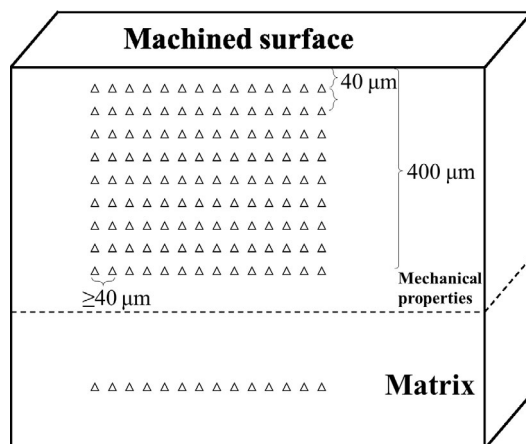

Fig. 1   Distribution of nanoindentation points.

of 1,250 HV1, and line roughness (R_a) of 20 nm. Before the wear test, the test surfaces of the original and 2D-USBP treated samples were polished until the surface roughness (S_a) was in the range of 50–100 nm. The counterparts and test samples were put into an ultrasonic cleaning machine for vibration cleaning with a purity of 99% alcohol for 10 min. Then, the two were placed in the vent to air dry. The following parameters were used for the wear tests: The applied load = 5.0, 10.0, and 15.0 N, the sliding speed = 12.56 mm/s, the sliding circle diameter = 4 mm, and the test time = 1,800 s. Three parallel wear tests were performed on the samples before and after machining at each set of wear parameters. The maximum Hertzian contact pressures in the wear tests with loading forces of 5, 10, and 15 N were 1,065, 1,342, and 1,536 MPa, respectively. The real-time acquisition of the coefficient of friction (COF) signal was undertaken at a sampling frequency of 300 Hz. Characterization of the wear scars was accomplished using white light interferometry and SEM.

2.4   MD simulation

A single-grain MD model (Fig. 2(a)) and a gradient-grain MD model (Fig. 2(b)) are established to study the effect of grain boundaries on the wear process. The two model consists of the fixed layer, the constant temperature layer, and the Newton layer. The constant temperature layer that controls the thermal equilibrium state of the models, approximately 300 K, is maintained by applying a velocity calibration method, thereby emulating the experimental temperature conditions. Atoms within the established Newton layer are subject to the governing laws of the potential function, whose kinetic behavior mirrors the atomic displacement characteristic of the wear process. The gradient-grain MD model has two grain boundaries within the model due to the misorientation, dividing the model into three grains. The simulation parameters of the two MD models are listed in Table 2.

2.5   CP simulation

The CP models have been successfully used to predict the mechanical response of materials under different loading environments [21–23]. As shown in Fig. 3, the 2D CP models, including a single-grain CP model
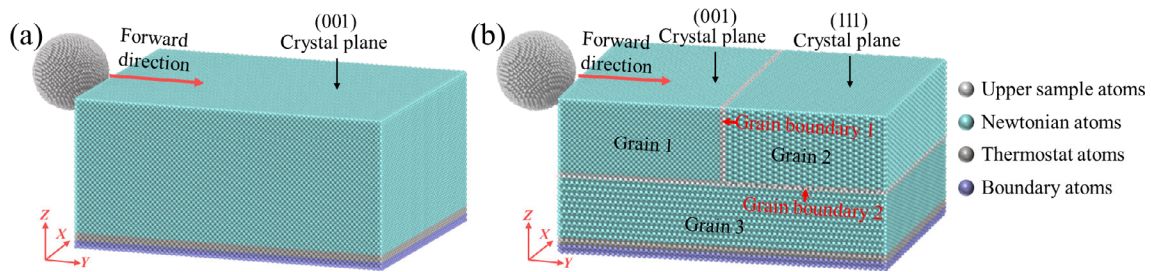
Fig. 2 MD models used for simulation of wear process: (a) single-grain MD model and (b) gradient-grain MD model.

Table 2 Simulation parameters of MD models.

Index	Parameter
Matrix	The single-grain MD model and the gradient-grain MD model
Matrix size (nm × nm × nm)	25.69 × 20.03 × 11.94 (contains about 384 thousand atoms)
Boundary condition	Free boundaries in the *X*-axis and *Z*-axis directions and periodic boundary conditions in the *Y*-axis direction
Al–Al potential function	The embedded atom method (EAM) potential function developed by Zhou et al. [19]
Al–C potential function	The L–J potential function developed by Yu et al. [20]
Counterpart	Diamond
Counterpart diameter (nm)	6 (contains about 20 thousand atoms)
Press-in depth (nm)	3.0
Sliding speed (Å/ps)	2

and a gradient-grain CP model, were established jointly with ABAQUS 2018 (Dassault Systèmes) and DAMASK 2.03 (Max-Planck-Institut für Eisenforschung GmbH) [24] software to explore the resistance mechanism of the gradient structure on wear. Each color block in the gradient-grain CP model represents a grain with a random crystal texture. A dislocation density-based constitutive model implemented in DAMASK was selected as the constitutive model [25]. The counterpart in the CP models was set as a rigid body with a spherical crown of 4 mm in diameter. The simulation parameters for the two CP models are listed in Table 3, in which the press-in depth of the spherical crown is obtained from the elastic–plastic simulation based on the mechanical properties of the original and 2D-USBP treated samples.

3 Results

3.1 Microstructure

The high-angle grain boundaries (HAGBs; the misorientation greater than 15°), low-angle grain boundaries (LAGB; the misorientation in 2°–15°), and

dislocation cells (DCs) on the cross-section of the 2D-USBP treated sample are plotted in Fig. 4(a), where the grains are colored according to the equivalent radius. HAGBs are colored with the blue lines, LAGBs are colored with the red lines, and DCs are colored with the cyan lines. The data in Fig. 4(a) are obtained by the EBSD. To elucidate the microstructural variations at disparate depths of the cross-section, an amplified view has been provided for distinct regions: the upper and lower regions of the refined grain layer (regions 1 and 2, respectively), the transition zone (region 3), and both the upper and middle regions of the coarse grain layer (regions 4 and 5, respectively). Furthermore, an area located 1 mm beneath the machined surface has been partitioned into ten separate segments for more detailed analysis. Then, the weighted average of the grain equivalent radius, the total length of HAGB, the total length of the LAGB, and the total length of the DC were counted for each part, whose results are presented in Figs. 5(a)–5(c).

In combination with Figs. 4 and 5, it can be observed that in region 1, the grain equivalent radius is about 1.8 nm; only a few DCs exist within the grains, and the grain boundary types are mainly dominated by
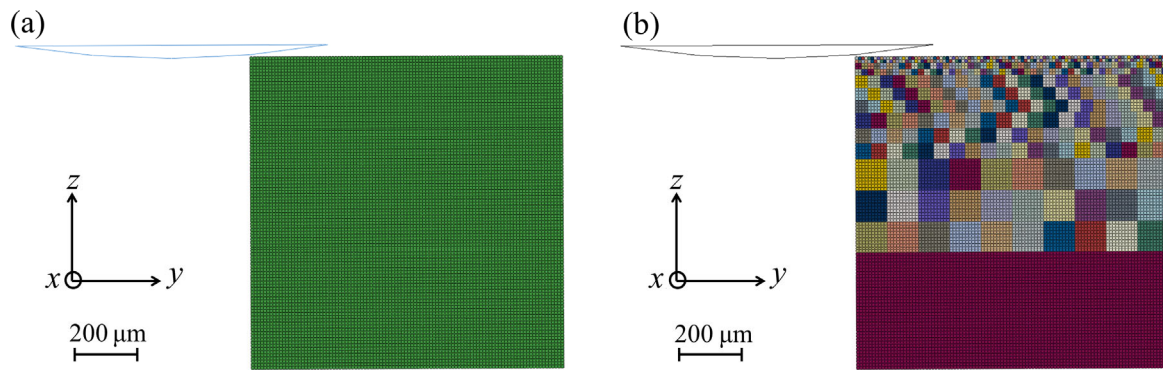
Fig. 3 ABAQUS–DAMASK mesh used for simulation of wear process: (a) single-grain CP model and (b) gradient-grain CP model.

Table 3 Simulation parameters of CP models.

Index	Single-grain CP model	Gradient-grain CP model
Matrix size (mm × mm)	1 × 1	1 × 1
Matrix mesh	10,000, CPE4R	10,000, CPE4R
Diameter of spherical crown (mm)	4	4
Press-in depth of spherical crown (μm)	3.68	3.21
Sliding speed (mm/s)	12.56 (towards the positive direction of the Y-axis)	12.56 (towards the positive direction of the Y-axis)
Contact condition	Coulomb friction	Coulomb friction
COF	0.422	0.383
Boundary condition	Model lower bound $U_1 = 0$ and $U_2 = 0$	Model lower bound $U_1 = 0$ and $U_2 = 0$
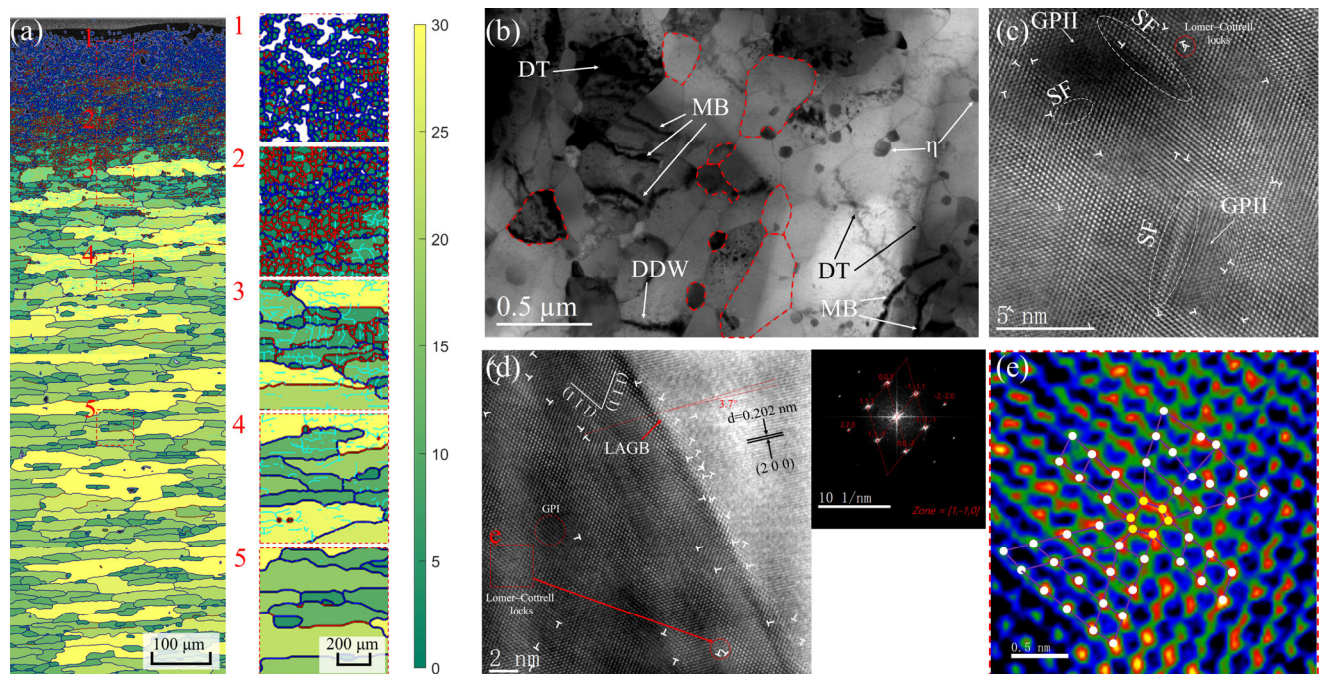
Fig. 4 Cross-sectional microstructures of 2D-USBP treated sample: (a) EBSD results, (b) TEM image (DT, DDW, and MB are the abbreviations of dislocation tangle, dense dislocation wall, and microband, respectively), (c) HRTEM image of stacking faults (SFs) and Ginnier–Preston II (GPII) zones, (d) HRTEM image of LAGB, and (e) magnified result of Lomer–Cottrell lock in (d).

the HAGB. In region 2, the grain equivalent radius does not grow significantly, but the grain boundary types gradually transition from HAGB to LAGB. Meantime, the number of DCs within the grains increases. In region 3 in Fig. 4(a), the grain equivalent radius increases rapidly with the increasing depth, the grain boundary types are mainly HAGB and LAGB, and many DCs exist within the grains. In region 4 in Fig. 4(a), the grains have a large equivalent radius, while the DCs within the grains are significantly reduced compared to those in region 3. In region 5 in Fig. 4(a), the grains reach the original size, while DCs are almost absent within the grains.

The DC and grain boundary distribution characteristics are mainly generated due to the crystal movement inside the sample during machining. At the beginning of the machining process, numerous dislocations are generated below the sample surface under large shear stress produced by the burnishing tool, which spontaneously forms DCs with lower energy. During machining, the continuous accumulation of dislocations sharpens the boundaries of DCs to form the LAGB. As the machining progresses, the misorientation on both sides of the LAGB gradually increases, becoming the HAGB. The high-density grain boundary on the surface consumes multitudinous DCs and limits the further generation of DCs, resulting in a low density of DCs in the surface layer. In the 0–100 μm region, the sample undergoes violent plastic deformation, transforming many LAGBs into HAGBs. The machining stress gradually decays with the increasing distance from the machined surface, weakening the crystalline motion inside the sample and resulting in the microstructure, as shown in Fig. 4(a).

Since the sampling step of the EBSD is only 0.9 μm,

the nano-sized grains on the sample surface cannot be identified. Figure 4(b) shows a TEM image of the microstructure on the surface of the 2D-USBP treated sample, in which the grains with clear partial grain boundaries are colored with the red dotted lines. The grain size of the machined surface is concentrated in 80–500 nm, so the surface grains belong to the mixed distribution of nano-grains and ultra-fine grains. Meanwhile, dislocation tangles (DTs), dense dislocation walls (DDWs), and microbands (MBs) can be observed inside the grains, produced by the intense plastic deformation of the surface layers during machining.

Furthermore, Figs. 4(c)–4(e) show the HRTEM images of the microstructures on the machined surface. Figure 4(c) shows that the GPII zones in the machined surface and its stress field can interact with dislocations and SFs, making them gather near the GP zone, hindering the movement of dislocations, and playing the role of the second-phase reinforcement. Figure 4(d) shows the HRTEM image of the surface LAGB, whose misorientation is 3.7° measured from the [200] direction of the adjacent grains, consisting of a series of ordered arrangements of dislocations and Lomer–Cottrell locks. The Lomer–Cottrell lock in Fig. 4(d) is enlarged, whose results are shown in Fig. 4(e). The Lomer–Cottrell lock within the surface nanocrystal can improve the work-hardening capability and improve the plasticity of the surface material at the same time. Overall, 2D-USBP prepared a gradient nanostructure of ~600 μm thick on the aluminum alloy surface, whose grain size and grain boundary length gradually increased with depth.

3.2 Hardness and elastic modulus

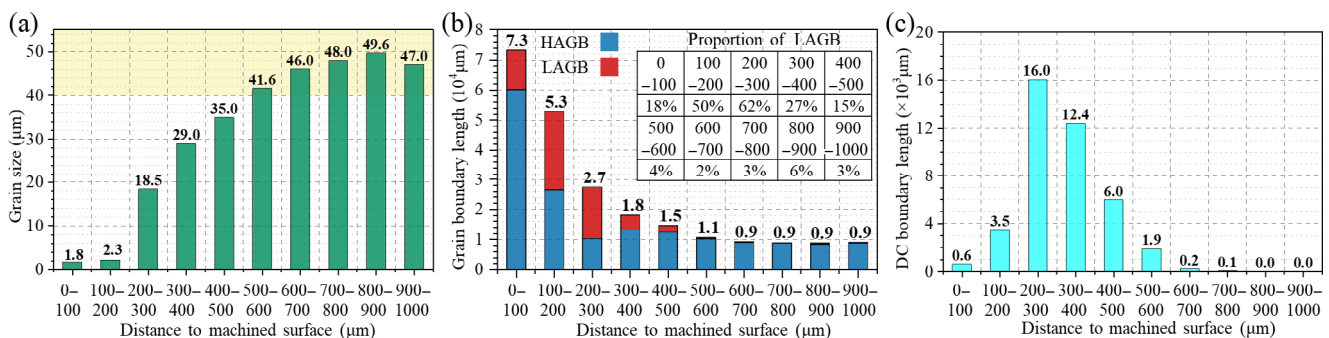Figure 6 shows the hardness and the elastic moduli

Fig. 5 Statistical results at different depths: (a) weighted average of grain equivalent radius, (b) grain boundary length, and (c) DC boundary length.
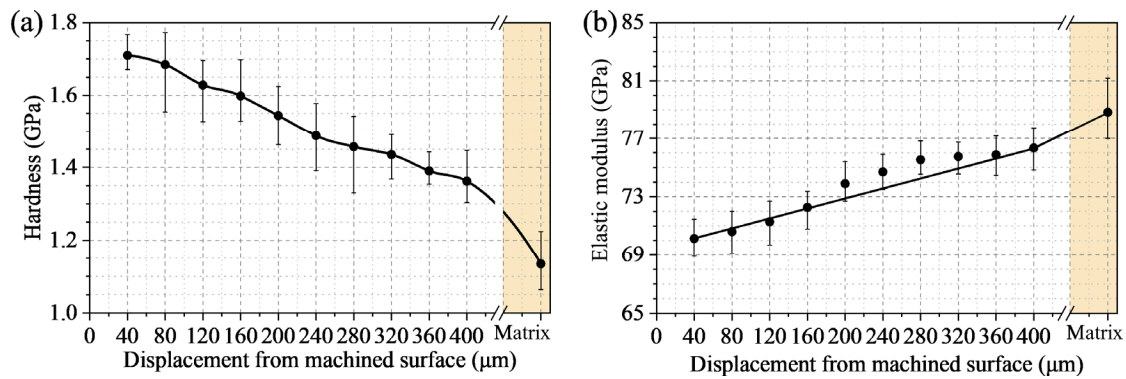
Fig. 6 Hardness and elastic moduli on cross-section of 2D-USBP treated sample: (a) hardness and (b) elastic moduli.

of the cross-section of the 2D-USBP treated sample. As the test point of nanoindentation moves closer to the machined surface from the matrix, the hardness increases from 1.13 to 1.71 GPa, and the elastic modulus decreases from 78.84 to 70.14 GPa, both of which are gradient distributions. The 2D-USBP sample machined gradient nanostructures on the sample surface, whose grain boundary ratio decreases as the depth from the machined surface increases. The elastic modulus measures the ability of an object to resist the elastic deformation from a macroscopic point of view and reflects the bonding strength between atoms, ions, or molecules from a microscopic point of view [26]. The atomic arrangement in the grain boundary is irregular, the lattice distortion is severe, the atomic spacing is increased, and the grains on both sides of the grain boundaries are different in orientation. The grain boundaries play a role in hindering the plastic deformation of the material, increasing the strength and hardness of the material. Meanwhile, a high proportion of grain boundaries also reduces the elastic modulus.

3.3 Wear scar

Figures 7(a)–7(c) show the temporal evolution of the COF for pre and post-machining samples under applied loads of 5, 10, and 15 N. In the initial phase of the wear test, the COFs for both sets of samples were in the range of 0.7–0.8. With the progression of wear duration, the COFs exhibit a gradual decrement, ultimately reaching a phase of stability. The wear of the two sample classes gradually transitioned from the running-in wear stage to the stable wear stage. It can be observed that the COFs of the original and 2D-USBP treated samples have similar magnitudes and trends over the wear time of 0–1,200 s under different loads, meaning that the 2D-USBP do not reduce the COF in the early wear, which is consistent with those reported by Rupert and Schuh [27], Argibay et al. [28], Padilla et al. [29], and Prasad et al. [30]. However, when the wear time is in the range of 1,500–1,800 s, the wear process of both sample classes under 5, 10, and 15 N loads is in the stable wear stage with the average COFs of 0.507, 0.438, and 0.422,
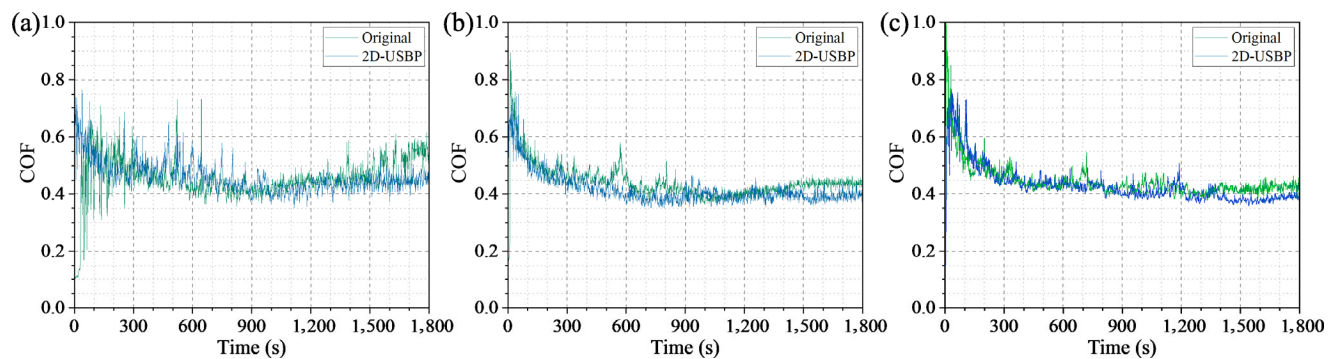

Fig. 7 COF–time curves under different loads: (a) 5 N, (b) 10 N, and (c) 15 N.

respectively, for the original samples and 0.449, 0.391, and 0.383, respectively, for the 2D-USBP treated samples. In time, the COFs of the 2D-USBP treated samples are smaller than those of the original samples, which may be related to the deterioration of the three-dimensional (3D) surface topography and the increase of the surface roughness of the worn surface for the original sample after prolonged wear.

Figure 8(a_1)–8(a_3) show the 3D morphologies of the wear scars for the original samples under 5–15 N loadings, Figs. 8(b_1)–8(b_3) show the 3D morphologies of the wear scars for the 2D-USBP treated samples, and Figs. 8(c_1)–8(c_3) compare the wear scar cross-sections of the two sample classes. Three parallel wear tests were performed on the original and 2D-USBP treated samples under each loading. The four positions were selected to measure the cross-sectional areas of the wear scars obtained from the wear tests, whose

statistical results are listed in Fig. 9. Under the loadings of 5, 10, and 15 N, the cross-sectional areas of the wear scars for the original samples are 41,080, 53,563, and 61,296 μm^2, respectively, and the 2D-USBP treated samples are 16,923, 20,929, and 33,453 μm^2, respectively. The wear area of the 2D-USBP treated sample is only about half of that of the original sample, meaning that 2D-USBP greatly improves the wear resistance.

When worn, the coarse grains on the original sample (Fig. 10(a)) and the gradient nanostructure on the 2D-USBP treated sample (Fig. 10(b)) have different response states, causing differences in the wear mechanism and antiwear properties between the two. In practical wear processes, multiple wear modalities are typically concurrent, with one form often instigating other variants of wear.

Figure 11(a_1) shows the surface morphology and element distributions of the wear scar of the original
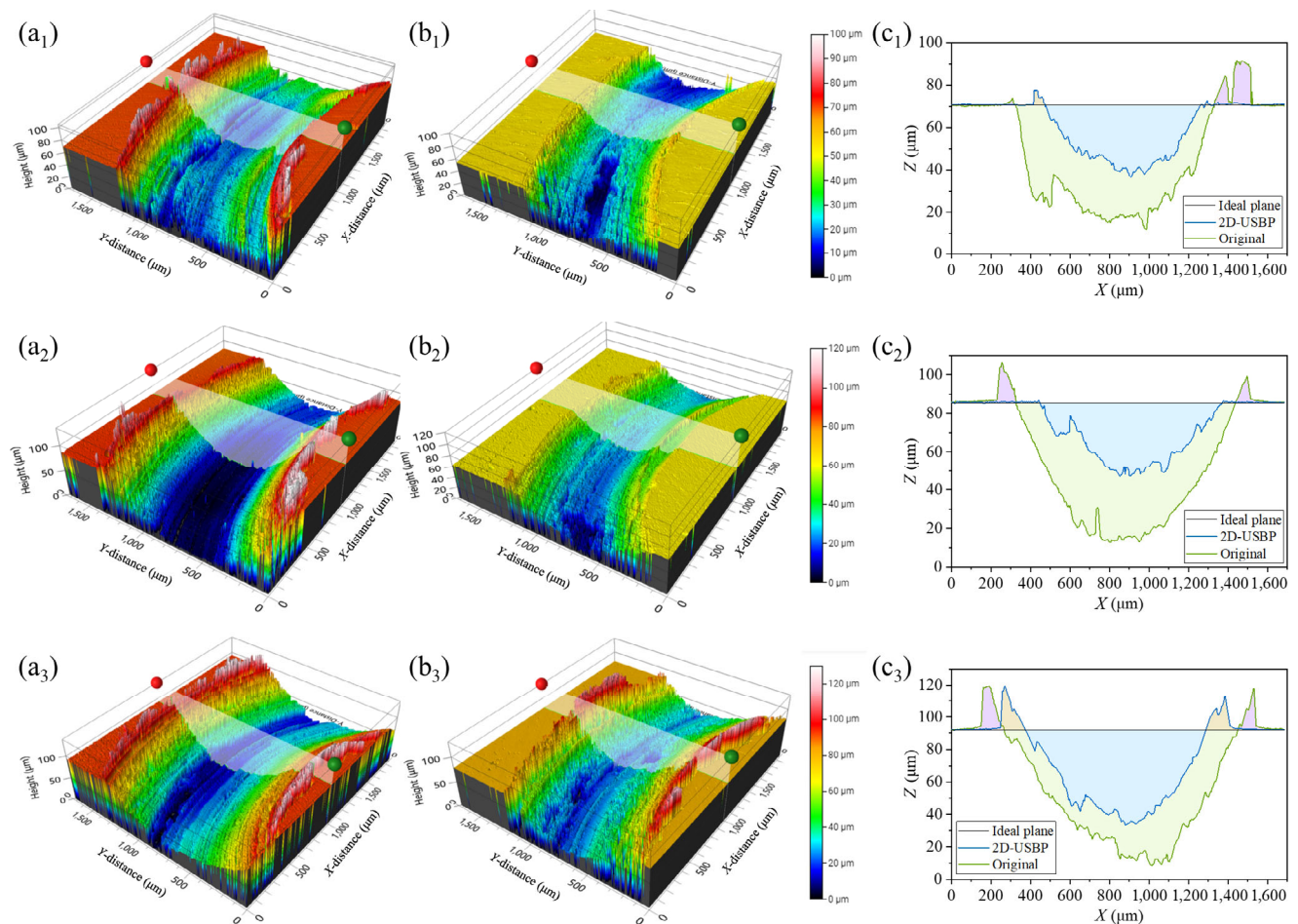

Fig. 8 3D morphologies of wear scars: (a_1–a_3) original samples under 5, 10, and 15 N, (b_1–b_3) 2D-USBP treated samples under 5, 10, and 15 N, and (c_1–c_3) wear areas under 5, 10, and 15 N.
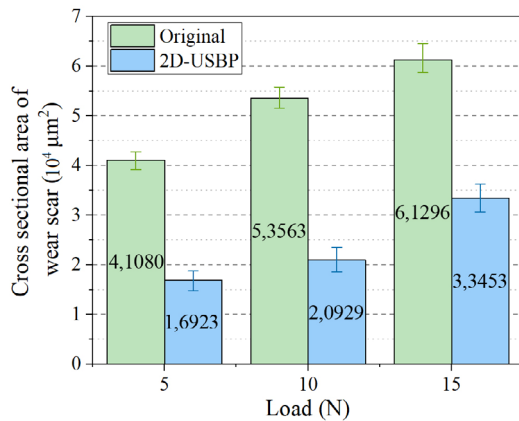
Fig. 9 Cross-sectional areas of wear scars under 5, 10, and 15 N.

sample under a 15 N load, and Fig. 11(a_2) shows the partial enlargement of the typical wear morphologies. The energy dispersive spectroscopy (EDS) results in Fig. 11(a_1) show that the worn surface of the original sample is enriched with oxygen atoms, with an atomic percentage of 36.94%. During the wear process, significant oxidative wear occurred. Figure 11(a_2) shows that many arc-shaped grooves are produced on the worn surface along with irregular adhesive regions, and some abrasive particles have been pressed into the worn surface due to the low hardness of the original sample surface. The grooves formed on the worn surface by the plowing action of the counterpart are wide and deep. The ridges formed beside the plowing grooves become flattened and eventually fracture after repeated loading and unloading cycles. Meanwhile, the contact occurs first on several micro-convex bodies in the wear process, causing adhesive at local pressures well above the yield pressure
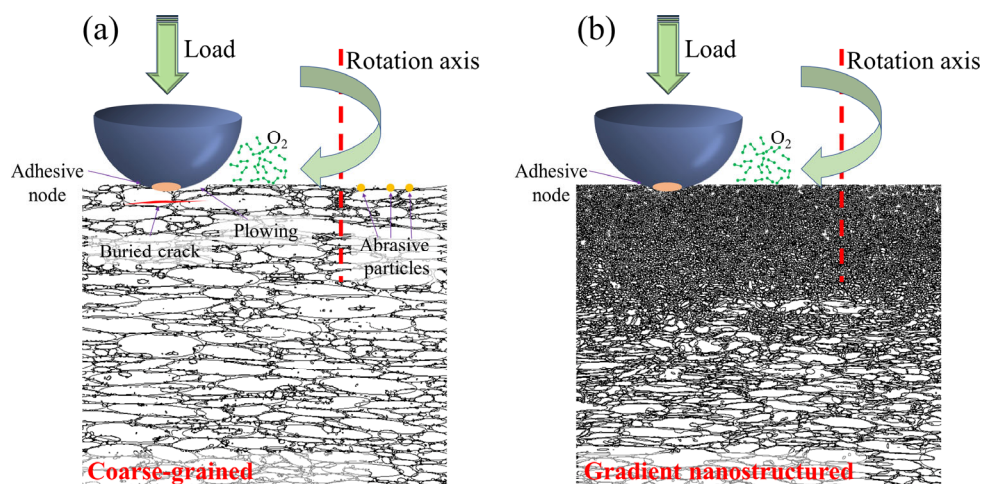
and tearing the adhesive points during subsequent sliding. Due to adhesive, the surface materials are stripped, as shown in the red dotted frame in Fig. 11(a_2). In addition, tiny cracks can be observed on the worn surface, and buried cracks can also be observed in the cross-section (Fig. 12(a)), causing deeper spalling.

Figure 11(b_1) shows the surface morphology and element distributions of the wear scar for the 2D-USBP sample under 15 N load, and Fig. 11(b_2) shows the partial enlargement of the typical wear morphologies. Figure 11(b_1) shows that the worn surface of the 2D-USBP treated sample is enriched with oxygen atoms, with an atomic percentage of 40.23%. Compared with that of the original sample, the worn surface of the 2D-USBP treated sample is smoother, and buried cracks are not observed in the cross-section (Fig. 12(b)). The regions of adhesive wear are present on the worn surface, along with slight grooves and ridges. Meanwhile, there is a certain delamination phenomenon in some regions on the worn surface, which can be explained by the delamination of the oxide layer.

The two sample classes coexist in multiple wear forms, where the original sample is dominated by oxidative and abrasive wear with adhesive wear, and the 2D-USBP treated sample is oxidative wear with adhesive wear.

4 Discussion

4.1 Gradient structure
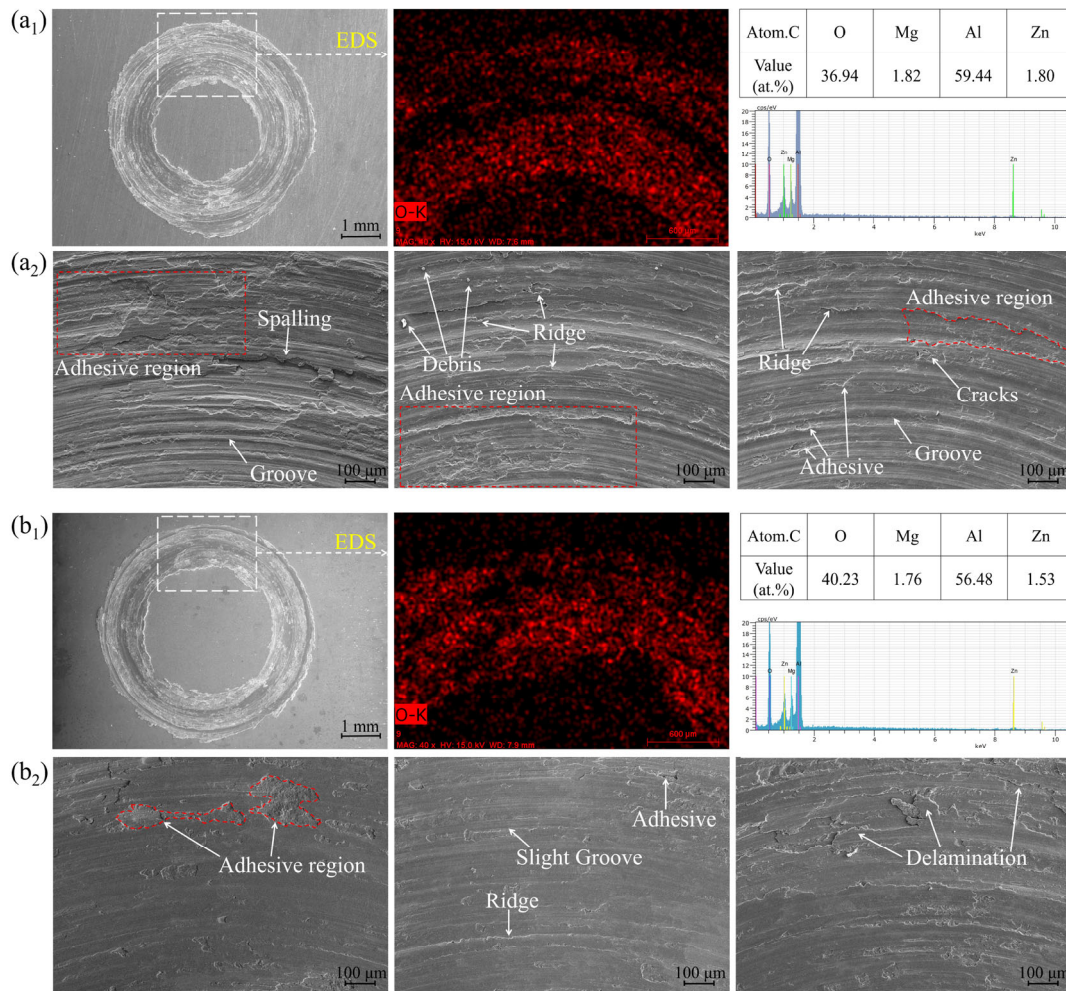
In summary, 2D-USBP effectively enhances the wear

Fig. 10 Schematic diagrams of wear process. (a) Original and (b) 2D-USBP treated samples.

Fig. 11 Surface morphologies of wear scars under 15 N load: (a$_1$, a$_2$) overall and local wear scars of original sample, respectively and (b$_1$, b$_2$) overall and local wear scars of 2D-USBP treated sample, respectively.
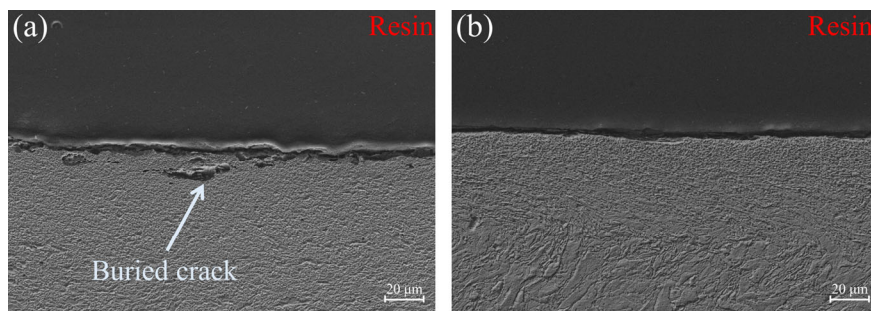

Fig. 12 Cross-section morphologies of wear scars under 15 N load: (a) original and (b) 2D-USBP treated samples.

resistance of the aluminum alloy. Wear is the most common equipment failure mode and is highly complex and sensitive. Unfortunately, due to the complexity and nonlinearity of the microstructure in metal materials, it is difficult to *in situ* observe the mechanism of the gradient structure machined by 2D-USBP on the wear enhancement by the experimental methods.

Comparing the simulation results of the single-grain MD model and the gradient-grain MD model when the counterpart is at different positions, as shown in Fig. 13, the resistance mechanism of the gradient-grain to wear is discussed on a small scale. Figures 14(a) and 14(b) show the distributions of transient microscopic defects, including slip planes
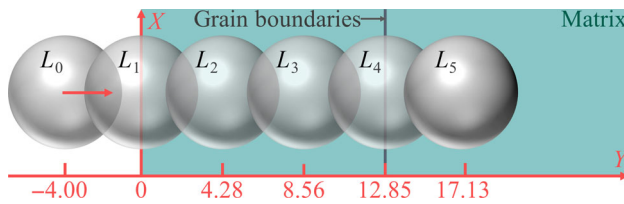
Fig. 13 Schematic diagram of counterpart in different positions. The spherical center of the counterpart is used as the position coordinate, and the left boundary of the matrix is set as 0 coordinates. The response of the matrix is discussed when the counterpart is located at −4 nm (L_0), 0 nm (L_1), 4.28 nm (L_2), 8.56 nm (L_3), 12.85 nm (L_4), and 17.13 nm (L_5). When the counterpart is located at L_0, the counterpart and the matrix are not in contact. The grain boundary 1 in the matrix is approximately 12.85 nm from the left boundary of the matrix. Therefore, when the counterpart is located at L_1, L_2, L_3, and L_4, the counterpart is situated at the left boundary of grain 1, one-third of grain 1, two-thirds of grain 1, and directly above the grain boundary 1, respectively. When the counterpart is located at L_5, the counterpart is positioned at one-third of grain 2.

and dislocations, within the single-grain MD model and the gradient-grain MD model during wear, respectively. Figures 15(a) and 15(b) show the potential energy distributions within the single-grain MD

model and the gradient-grain MD model during wear, respectively. Figures 16(a) and 16(b) show the von-Mises stress distributions within the single-grain MD model and the gradient-grain MD model during wear, respectively.

Figure 14 shows that when the counterpart is located at $L_0 = -4$ nm, the counterpart is not yet in contact with the two models, where no dislocations are generated. Figures 15 and 16 show that the distributions of the potential energy and von-Mises stress, respectively, in the single-grain MD model are relatively uniform, and the gradient-grain MD model has higher von-Mises stress and potential energy at the grain boundaries. When the counterpart moves to $L_1 = 0$ nm, the counterpart exerts large stress on the two models in the advancing direction, causing dislocations to multiply and slip from the contact area. The dislocations in the single-grain MD model are distributed over a wide range, well beyond the distance traveled by the counterpart. In contrast, the dislocations in the gradient-grain MD model are confined within grain 1 on the upper left.
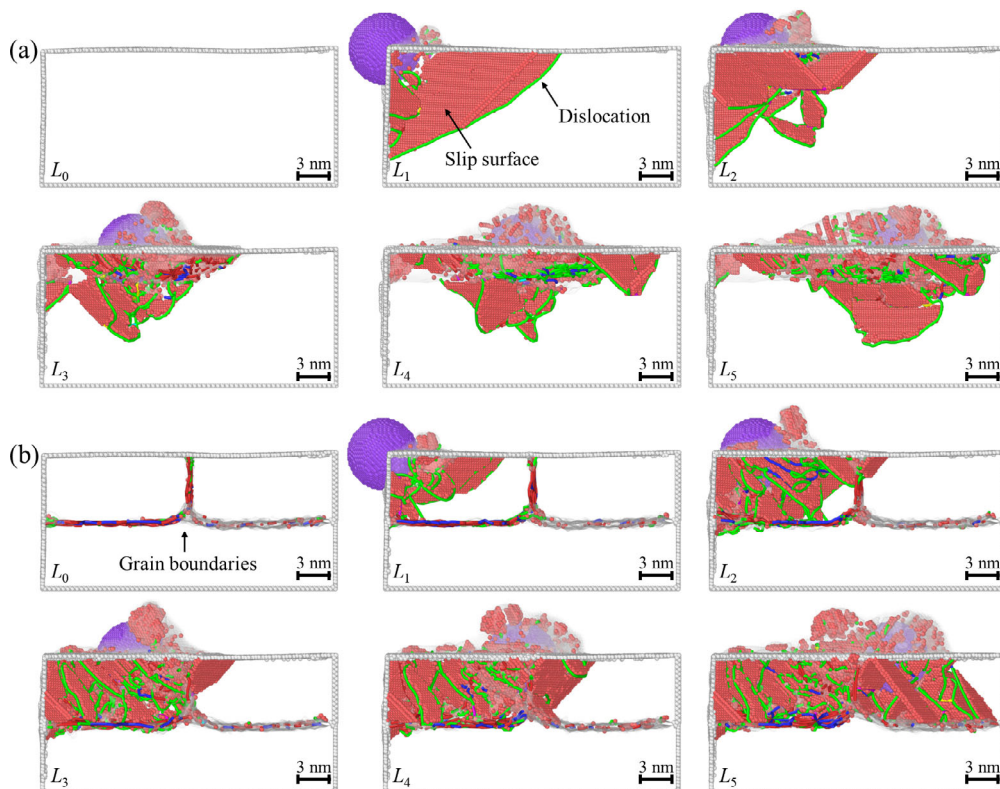

Fig. 14 Instantaneous microscopic defect distributions in the wear process: (a) single-grain MD model and (b) gradient-grain MD model.
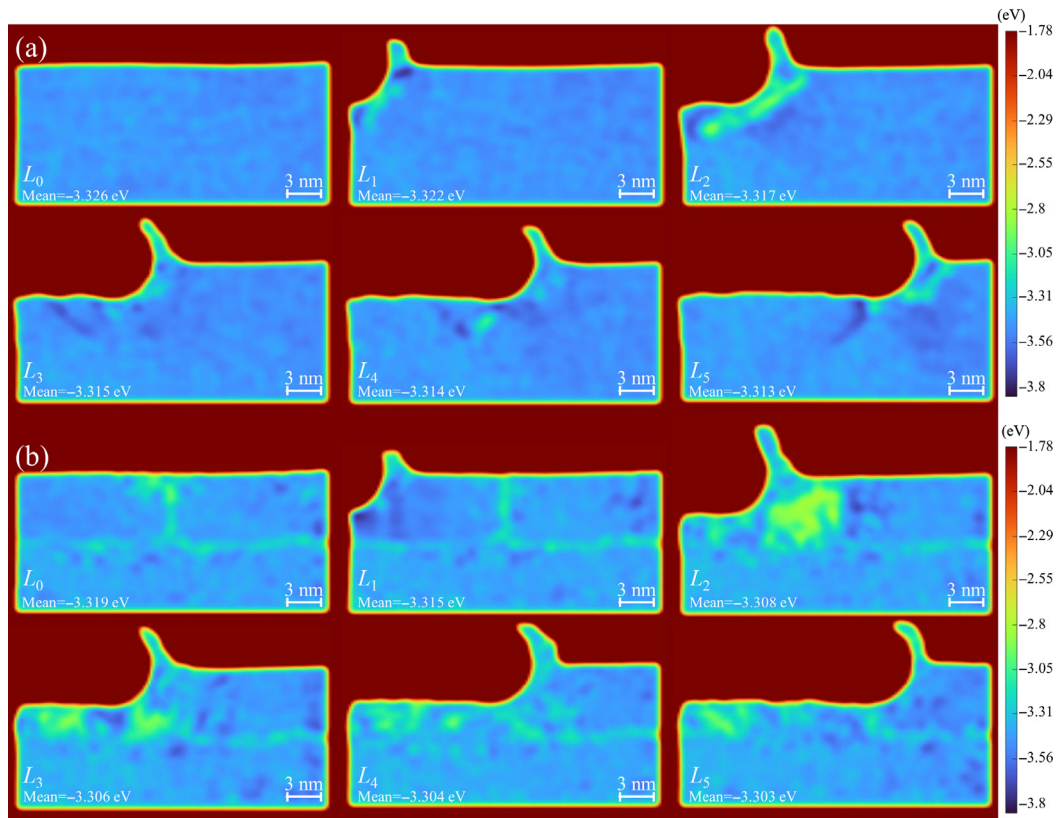
Fig. 15 Potential energy distributions in the wear process: (a) single-grain MD model and (b) gradient-grain MD model.
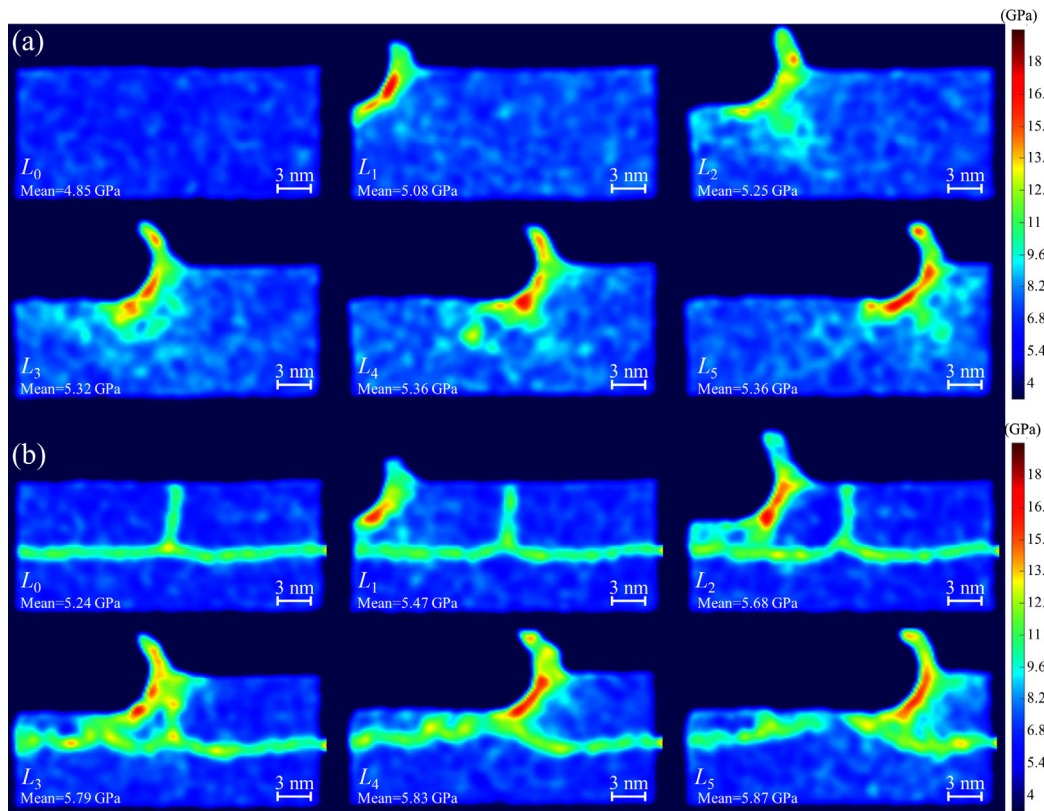

Fig. 16 Von-Mises stress distributions in the wear process: (a) single-grain MD model and (b) gradient-grain MD model.

Figure 17 shows the total dislocation length–counterpart displacement curves of the two models during the simulation. The different starting points of the vertical ordinates for the two curves are due to partial dislocations within the grain boundaries of the gradient-grain MD model, so the changes in the dislocation length can be visually compared by translating the vertical ordinates. When the counterpart moves to L_1, there is no significant difference in the total length of dislocations between the two models, i.e., the gradient-grain boundary only inhibits the dislocation slip and has no significant effect on the dislocation multiplication.

Figure 18 shows the potential energy–counterpart displacement curves in the two models during wear, again by translating the vertical ordinates to visually compare the potential energy growth between the two models. It can be observed that the potential energy of both models gradually increases with the motion of the counterpart, but the increase is very close, meaning that the counterpart has almost the same energy input for both models. When the counterpart moves to L_2 = 4.28 nm and L_3 = 8.56 nm, new dislocations inside the single-grain MD model
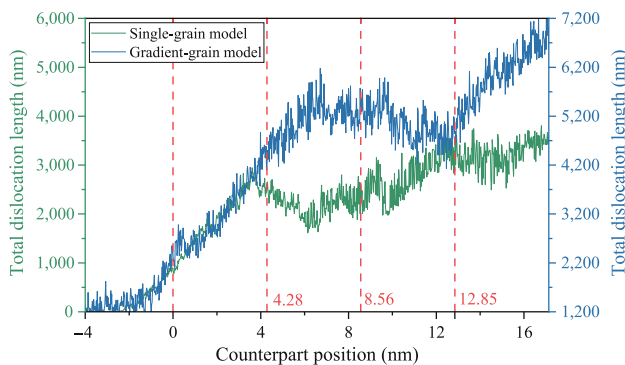

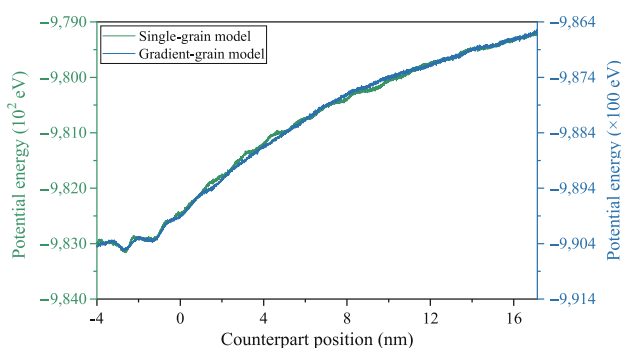**Fig. 17** Total dislocation length vs. counterpart displacement curves.

Fig. 18 Potential energy vs. counterpart displacement curves.

continuously nucleate in the contact area, and then slip along the {111} glide plane towards the advancing direction of the counterpart, in which some dislocations move to the free surface to form atomic steps leading to annihilation, so the total dislocation length does not increase significantly. The range of the large stress distribution in the single-grain MD model is significantly larger than that in the gradient-grain MD model, driving the dislocations of the single-grain MD model to slip inward continuously. Thus, the single-grain MD model produces a wider range of plastic deformation. Also, the potential energy distribution within the single-grain MD model is more uniform. In the gradient-grain MD model, grain boundaries block the dislocation slip within grain 1, producing an obvious dislocation pile-up. As the counterpart approaches the grain boundary, the energy input from the counterpart is confined within grain 1 by the grain boundary, which has higher potential energy, resulting in more dislocations, and the total dislocation length is significantly larger than that of the single-grain MD model. At the same time, the stress generated in the model by the counterpart drives part dislocations to cross the grain boundaries and slips within grain 2.

When the counterpart moves to L_4 = 12.85 nm, it is above grain boundary 1. The dislocations within the single-grain MD model are distributed throughout the model. In the gradient-grain MD model, the space between the counterpart and the grain boundary is continuously compressed when approaching the grain boundary, where produces high potential energy and stress, forcing dislocations to slip toward the grain boundary. Therefore, numerous dislocations are absorbed and annihilated by the grain boundary, resulting in a significant reduction of the total dislocation length in the gradient-grain MD model. Numerous dislocations and grain boundaries interact in the gradient-grain MD model, so the motion of dislocations is still limited to a small space.

When the counterpart moves to L_5 = 17.13 nm, it traverses the position of grain boundary 1. The dislocations in the single-grain MD model glide in a direction congruent with the advancement of the counterpart. Contrariwise, although the dislocations in the gradient-grain MD model also advance in the direction of the counterpart's movement, the

dislocation distribution is confined within grain 1 and grain 2, exhibiting a smaller depth of influence. Figures 14–18 visualize that the input energy from the counterpart to the two models is similar during the simulation process. However, the gradient-grain MD model successfully confines the distribution of contact stress and potential energy within a diminutive range, consequently restricting plastic deformation to a relatively minor region within the surface layer. It is a factor that significantly enhances the overall wear resistance.

In addition, the mechanism of gradient-grain on the wear resistance enhancement is further discussed by comparing the simulation results of the single-grain CP model and the gradient-grain CP model. Figure 19 shows the dislocation multiplication and annihilation distribution within the single-grain CP model and the gradient-grain CP model during the wear process. Figures 19(a_1) and 19(b_1) show that dislocations primarily multiply in the contact region of the two

models under the extrusion and shearing effect of the counterpart in the course of wear. Furthermore, the number and distribution range of dislocation proliferation in the two models are similar. Figures 19(a_2) and 19(b_2) show that the annihilation rate of dislocation in the gradient-grain CP model is much larger than that in the single-grain CP model, mainly attributed to the high density of grain boundaries in the surface layer, forcing numerous dislocations to be confined in a small space, increasing the probability of mutual annihilation of the opposite Burgers vector dislocations. Meantime, the grain boundary absorbs a part of the dislocations. The gradient-grain CP model has a large rate of dislocation annihilation to effectively suppress the possibility of cracking from dislocation accumulation.

Figure 20 shows the dislocation densities within the single-grain CP model and the gradient-grain CP model during the wear process. Comparing Figs. 20(a_1) and 20(b_1), the maximum movable dislocation density
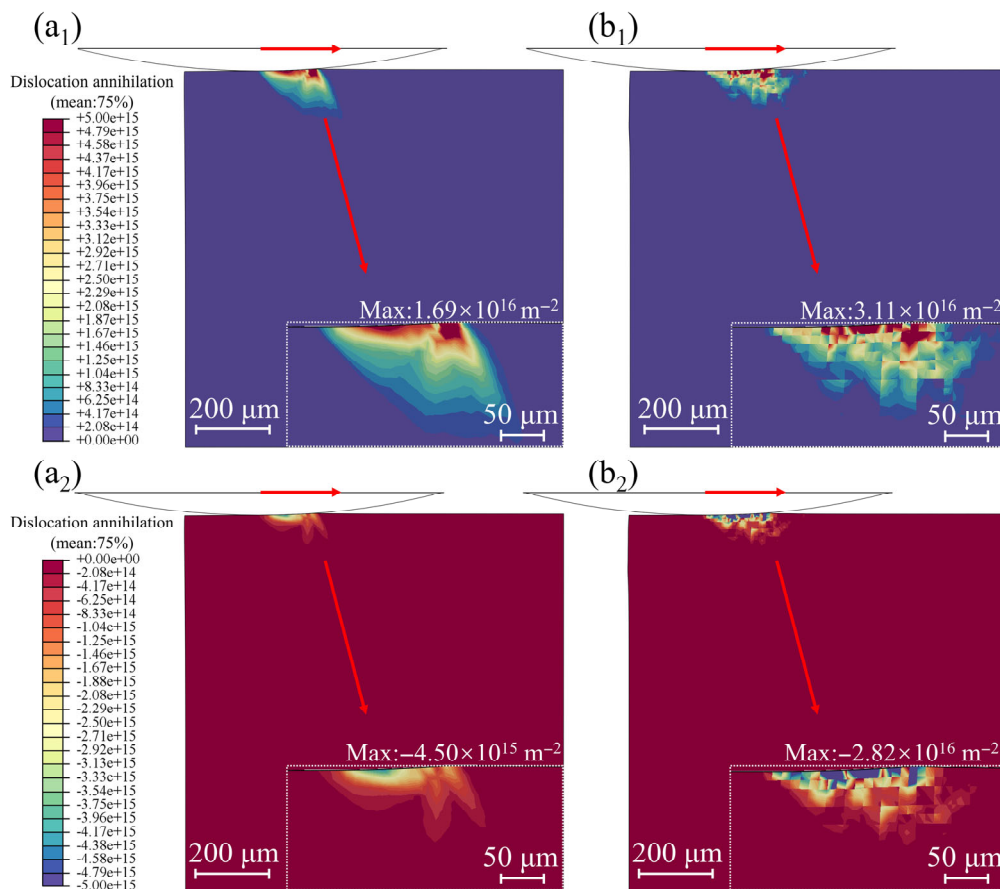

Fig. 19 Distributions of dislocation multiplication and dislocation annihilation in the wear process: (a_1, a_2) single-grain CP model and (b_1, b_2) gradient-grain CP model.
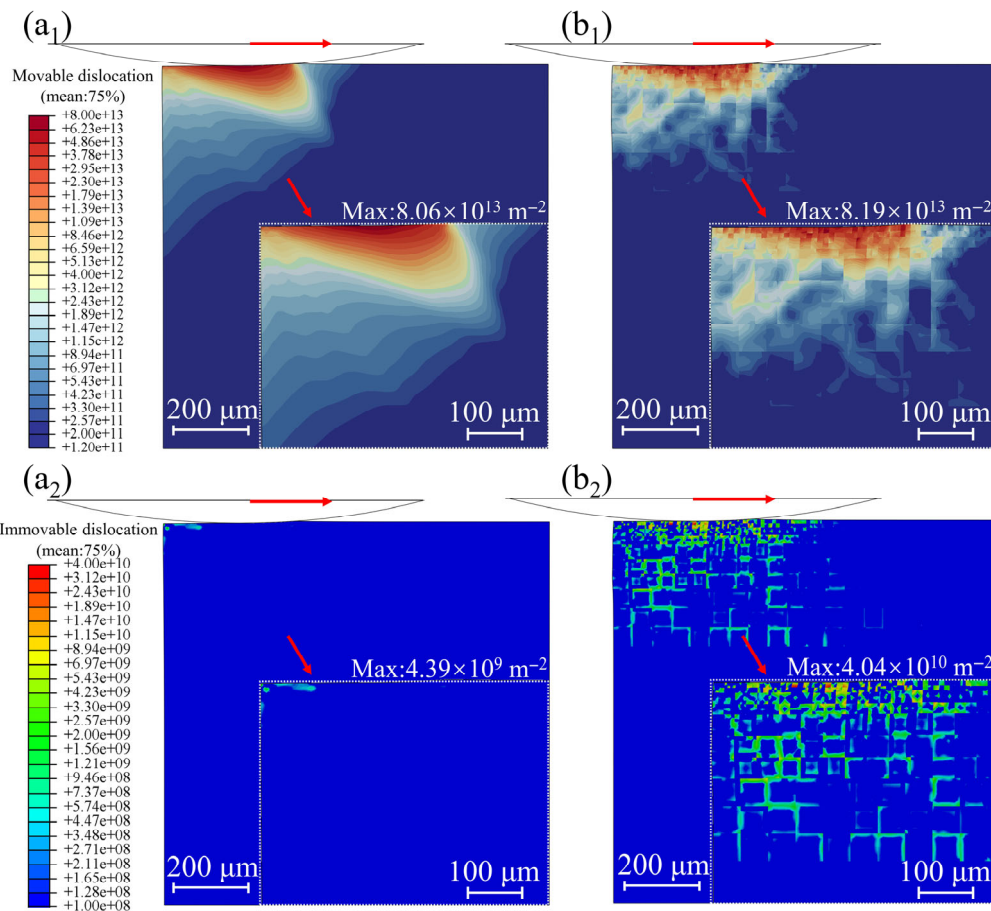
Fig. 20 Density distributions of movable and immobile dislocations in the wear process: (a₁, a₂) single-grain CP model and (b₁, b₂) gradient-grain CP model.

is 8.06×10^{13} m⁻² in the single-grain CP model and 8.19×10^{13} m⁻² in the gradient-grain CP model, respectively. The distribution of movable dislocation density within the single-grain CP model exhibits continuity. However, in the gradient-grain CP model, the movable dislocation density displays a discontinuous pattern, impeded by the high-density grain boundaries at the surface. Additionally, it can be observed that the range of the region with high movable dislocation density in the gradient-grain CP model is lesser than that in the single-grain CP model. It is primarily due to the constraining influence of grain boundaries on dislocation glide, as illustrated in Fig. 14. When the dislocation slips near the grain boundary, part of the dislocation is absorbed by the grain boundary, part of the dislocation piles up at the grain boundary to produce a stress concentration region, and part of the dislocation continues to slip through the grain boundary. Therefore, the high-density grain boundary beneath

the surface of the gradient-grain CP model effectively reduces the slidable range of dislocations, leading to a diminished region of plastic deformation on the model surface during wear, thereby enhancing the model surface's ability to resist plastic deformation.

Figures 20(a₂) and 20(b₂) show the density distributions of immovable dislocations in the single-grain CP model and the gradient-grain CP model, respectively. The immovable dislocations of the single-grain CP model are distributed in the near-surface area, where the model is in contact with the counterpart and has a small overall distribution range. The immovable dislocations of the gradient-grain CP model are mainly distributed at the grain boundaries. The movement of dislocations to the grain boundaries produces plugging, resulting in the transformation of many dislocations into immovable dislocations, which is the main reason for the delamination on the 2D-USBP treated sample.

4.2 Mechanical properties

Why wear occurs is that the material surface undergoes continuous loss, adhesion, crack initiation, and plastic deformation when the counterpart moves relative. In most working environments, the wear resistance of a material is directly determined by the microstructure and mechanical properties of its surface. The gradient nanostructure machined by 2D-USBP improves the surface mechanical properties, thus increasing the wear resistance.

Figure 21 shows the elastic strain (ε_e), the plastic strain (ε_p), the total strain (ε_t), and the recovery resistance on the cross-section of the 2D-USBP treated sample, identified from the nanoindentation results [31, 32]. As the test point of nanoindentation moves closer to the machined surface from the matrix, the ε_e tends to increase (Fig. 21(a)), the ε_p tends to decrease (Fig. 21(b)), the ε_t tends to increase (Fig. 21(c)), and the recovery resistance tends to decrease (Fig. 21(d)). The recovery resistance is an indicator of energy dissipation during nanoindentation. Energy dissipation is mainly due to plastic deformation, crack generation, and propagation. The decrease in the recovery resistance represents a decrease in surface plasticity, corresponding to the results of Fig. 21(b). Simultaneously, the fine-grained surface amplifies the surface layer's resistance to plastic deformation, thereby bolstering

its ability to resist blocking and shearing. The increase in hardness coupled with the decrease in plasticity can diminish the impact depth when the adhesive nodes succumb to destruction during wear. These factors account for the robust anti-adhesive wear properties exhibited by the 2D-USBP treated sample.

Furthermore, materials with higher hardness can reduce the penetration depth of the counterpart in the wear process, reducing the scope of counterpart furrowing and cutting. The elevated strain tolerance, as shown in Fig. 21(c), equips the worn surface with the capability to endure substantial deformation, facilitating the dispersion of contact stress concentration during wear, which correspondingly augments the worn surface's ability to foreign object intrusion. Also, the surface grain refinement allows more grains to participate in resisting the destructive effect of the counterpart movement and play the role of the overall defense.

As postulated by the energy wear theory, a fraction of the work accomplished during wear, specifically the work associated with plastic deformation, is conserved within the worn surface in potential energy. When the accumulated energy reaches the critical value, a certain volume of material peels off the surface as wear particles. Reducing the probability of crack initiation and propagation in the wear process
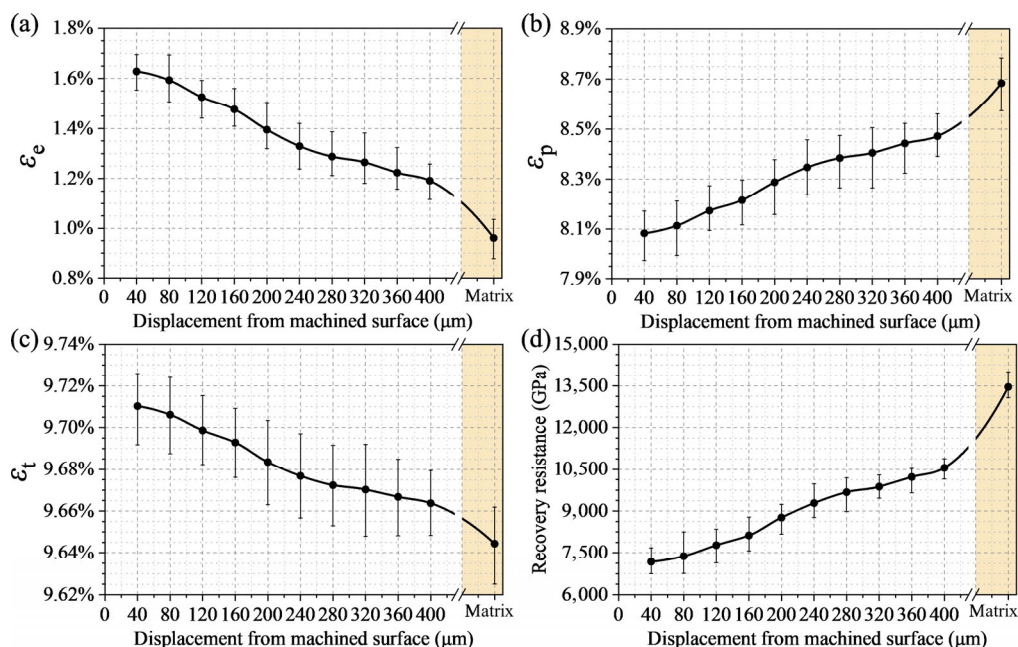

Fig. 21 Strain on cross-section of 2D-USBP treated sample: (a) ε_e, (b) ε_p, (c) ε_t, and (d) recovery resistance.

is necessary. The fracture toughness of materials is essential to crack initiation. W_e, an approximation representing the ratio of elastic strain energy to the total energy in the deformation of the material, is of key importance for developing the surface with enhanced toughness and resistance to cracking [33–35]. The quotient of hardness to elastic modulus (H/E) is a quantifiable measure of material fracture toughness, signifying the material's inherent capacity to impede crack propagation [36]. H^3/E^2 is proportional to the critical load that causes plastic deformation of the plane when a rigid ball is pressed into the plane, obtained by solving for the Hertz in contact mechanics [37].

Figure 22 shows the W_e on the cross-section of the 2D-USBP treated sample. As the depth from the machined surface decreases, the W_e increases from 12.6% to 19.1%. Figure 23 shows the H/E and H^3/E^2 on the cross-section of the 2D-USBP treated sample. As the depth from the machined surface decreases, the H/E has an increasing trend from 1.44×10^{-2} to 2.44×10^{-2} (Fig. 23(a)), and the H^3/E^2 has an increasing trend from 2.35×10^{-4} to 10.16×10^{-4} GPa (Fig. 23(b)).

The 2D-USBP increases the W_e, H/E, and H^3/E^2 in the surface layer, meaning that in the wear process,

the energy absorbed by the wear surface becomes less. There remain more elastic deformation components in the deformation of the contact peak on the wear surface, which can withstand wear for a longer time, to the extent that the ability of the wear surface to resist crack initiation and propagation is improved, as shown in Fig. 12. Under the same wear energy, the wear surface of the gradient nanostructure produces smaller plastic deformation and greater resistance to cracking, enhancing the wear resistance.

5 Conclusions

1) The 2D-USBP sample prepares a gradient nanostructure of ~600 μm thick on the aluminum alloy surface, whose grain size and grain boundary length gradually increase with depth. The grain size of the machined surface is concentrated in the range of 80–500 nm, and there are many DTs, DDWs, MBs, SFs, and Lomer–Cottrell locks within the grains. The hardness of the gradient nanostructure gradually increased from 1.13 GPa in the matrix to 1.71 GPa near the machined surface, and the elastic modulus decreased from 78.84 to 70.14 GPa, both in a gradient distribution.

2) After the wear tests under 5, 10, and 15 N loads, the cross-sectional areas of the wear scars for the original samples are 41,080, 53,563 and 61,296 μm^2, respectively, and the 2D-USBP treated samples are 16,923, 20,929, and 33,453 μm^2, respectively. The wear area of the 2D-USBP treated sample is only about half of that of the original sample, meaning that the 2D-USBP greatly improves the wear resistance. The two samples coexist with multiple wear forms, where the original sample is dominated by oxidative and
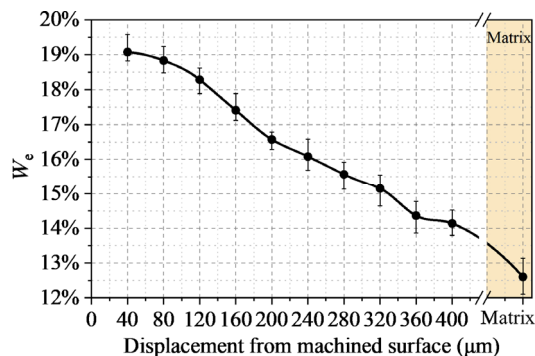

Fig. 22 W_e on cross-section of 2D-USBP treated sample.

Fig. 23 Cross-sectional parameters on the 2D-USBP treated sample: (a) H/E and (b) H^3/E^2.

abrasive wear with adhesive wear, and the 2D-USBP treated sample is oxidative wear with adhesive wear.

3) The gradient nanostructure limits the contact stress and potential energy distribution to a small range within the sample during the wear process. The high-density grain boundaries in the surface effectively reduce the distribution range of the dislocations, i.e., improving the plastic deformation resistance of the sample. The W_e, H/E, and H^3/E^2 of the machined surface are higher than those of the original surface, effectively enhancing the resistance to crack initiation and propagation of the sample. The increase in hardness and the decrease in surface plasticity effectively enhance the anti-adhesion ability of the 2D-USBP treated sample.

Availability of data and materials

The submitted article appears all data, models, and materials generated or used during the study.

Acknowledgements

Declaration of competing interest

The authors have no competing interests to declare that are relevant to the content of this article.

References

[1] Ni Y, Fu L, Shen Z, Liu X C. Role of tool design on thermal cycling and mechanical properties of a high-speed micro friction stir welded 7075-T6 aluminum alloy. *J Manuf Process* **48**: 145–153 (2019)

[2] Zhang S, Zhang T, He Y T, Du X, Ma B L, Zhang T Y. Long-term atmospheric pre-corrosion fatigue properties of epoxy primer-coated 7075-T6 aluminum alloy structures. *Int J Fatigue* **129**: 105225 (2019)

[3] Barooah R K, Arif A F M, Paiva J M, Oomen-Hurst S, Veldhuis S C. Wear of form taps in threading of Al–Si alloy parts: Mechanisms and measurements. *Wear* **442–443**: 203153 (2020)

[4] Fuentes R, Ono R, Nakajima N, Nishizawa H, Siswanto J, Aziz N, Sriwigati, Sofian H O, Miranda T, Pawlik A. Technological and behavioural complexity in expedient industries: The importance of use-wear analysis for understanding flake assemblages. *J Archaeol Sci* **112**: 105031 (2019)

[5] Chen Q P, Xie Q S, Yuan Q N, Huang H S, Li Y T. Research on a real-time monitoring method for the wear state of a tool based on a convolutional bidirectional LSTM model. *Symmetry* **11**(10): 1233 (2019)

[6] Sun H, Li A H, Zhou Y H, Liao X L, Ge D J. Dry wear characteristics of machined ZL109 aluminum–silicon alloy surface under unidirectional and reciprocating rolling-contact friction. *Surf Topogr Metrol Prop* **8**(1): 015001 (2020)

[7] Xie S Y, Li R D, Yuan T C, Chen C, Zhou K C, Song B, Shi Y S. Laser cladding assisted by friction stir processing for preparation of deformed crack-free Ni–Cr–Fe coating with nanostructure. *Opt Laser Technol* **99**: 374–381 (2018)

[8] Zhao X H, Zhao Y Q, Xu D S, Hu C H. Effect of gradient nanostructure on plasma sulfonitrocarburizing of 42MnCr52 steel. *Tribol Trans* **63**(1): 133–143 (2020)

[9] Ao N, Liu D X, Xu X C, Zhang X H, Liu D. Gradient nanostructure evolution and phase transformation of α phase in Ti–6Al–4V alloy induced by ultrasonic surface rolling process. *Mat Sci Eng A-Struct* **742**: 820–834 (2019)

[10] Wang X, Li Y S, Zhang Q, Zhao Y H, Zhu Y T. Gradient structured copper by rotationally accelerated shot peening. *J Mater Sci Technol* **33**(7): 758–761 (2017)

[11] Deng S Q, Godfrey A, Liu W, Hansen N. A gradient nanostructure generated in pure copper by platen friction sliding deformation. *Scripta Mater* **117**: 41–45 (2016)

[12] Ren Z J, Lai F Q, Qu S G, Zhang Y L, Li X Q, Yang C. Effect of ultrasonic surface rolling on surface layer properties and fretting wear properties of titanium alloy Ti$_5$Al$_4$Mo$_6$V$_2$Nb$_1$Fe. *Surf Coat Technol* **389**: 125612 (2020)

[13] Liu X, Zheng Y H, Guo Y L, Kong H J. Study on the rolling friction and wear properties of surface densified powder metallurgy Fe–2Cu–0.6C material. *Surf Topogr Metrol Prop* **8**(1): 015009 (2020)

[14] Liu X, Xiao Z Y, Guan H J, Zhang W, Li F L. Friction and wear behaviours of surface densified powder metallurgy Fe–2Cu–0.6C material. *Powder Metall* **59**(5): 329–334 (2016)

[15] Ma C, Andani M T, Qin H F, Moghaddam N S, Ibrahim H, Jahadakbar A, Amerinatanzi A, Ren Z C, Zhang H, Doll G L, et al. Improving surface finish and wear resistance of additive manufactured nickel-titanium by ultrasonic nano-crystal surface modification. *J Mater Process Tech* **249**: 433–440 (2017)

[16] Zhou Z Y, Zheng Q Y, Ding C, Yan J Y, Peng G J, Piao Z Y. Research on the promotion mechanism of surface burnishing process by two-dimensional ultrasonic vibration. *J Mater Res Technol* **13**: 1068–1082 (2021)

[17] Zhou Z Y, Zheng Q Y, Ding C, Yu G L, Peng G J, Piao Z Y. Investigation of two-dimensional ultrasonic surface burnishing process on 7075-T6 aluminum. *Chin J Mech Eng* **34**(1): 19 (2021)

[18] Niessen F, Nyyssönen T, Gazder A A, Hielscher R. Parent grain reconstruction from partially or fully transformed microstructures in MTEX. *J Appl Crystallogr* **55**(1): 180–194 (2022)

[19] Zhou X W, Johnson R A, Wadley H N G. Misfit-energy-increasing dislocations in vapor-deposited CoFe/NiFe multilayers. *Phys Rev B* **69**(14): 144113 (2004)

[20] Yu H L, Adams J B, Hector L G. Molecular dynamics simulation of high-speed nanoindentation. *Model Simul Mater Sc* **10**(3): 319–329 (2002)

[21] Han F B, Roters F, Raabe D. Microstructure-based multiscale modeling of large strain plastic deformation by coupling a full-field crystal plasticity-spectral solver with an implicit finite element solver. *Int J Plasticity* **125**: 97–117 (2020)

[22] Helm D, Butz A, Raabe D, Gumbsch P. Microstructure-based description of the deformation of metals: Theory and application. *JOM* **63**(4): 26–33 (2011)

[23] Lu X C, Zhang X, Shi M X, Roters F, Kang G Z, Raabe D. Dislocation mechanism based size-dependent crystal plasticity modeling and simulation of gradient nano-grained copper. *Int J Plasticity* **113**: 52–73 (2019)

[24] Roters F, Diehl M, Shanthraj P, Eisenlohr P, Reuber C, Wong S L, Maiti T, Ebrahimi A, Hochrainer T, Fabritius H O, et al. DAMASK—The Düsseldorf Advanced Material Simulation Kit for modeling multi-physics crystal plasticity, thermal, and damage phenomena from the single crystal up to the component scale. *Comp Mater Sci* **158**: 420–478 (2019)

[25] Roters F. Advanced material models for the crystal plasticity finite element method: Development of a general CPFEM framework. Postdoctoral Thesis. Germany: RWTH Aachen University, 2011.

[26] Thomason P F. Ductile spallation fracture and the mechanics of void growth and coalescence under shock-loading conditions. *Acta Mater* **47**(13): 3633–3646 (1999)

[27] Rupert T J, Schuh C A. Sliding wear of nanocrystalline Ni–W: Structural evolution and the apparent breakdown of Archard scaling. *Acta Mater* **58**(12): 4137–4148 (2010)

[28] Argibay N, Furnish T A, Boyce B L, Clark B G, Chandross M. Stress-dependent grain size evolution of nanocrystalline Ni-W and its impact on friction behavior. *Scripta Mater* **123**: 26–29 (2016)

[29] Padilla H A II, Boyce B L, Battaile C C, Prasad S V. Frictional performance and near-surface evolution of nanocrystalline Ni–Fe as governed by contact stress and sliding velocity. *Wear* **297**(1–2): 860–871 (2013)

[30] Prasad S V, Battaile C C, Kotula P G. Friction transitions in nanocrystalline nickel. *Scripta Mater* **64**(8): 729–732 (2011)

[31] Milman Y V, Golubenko A A, Dub S N. Indentation size effect in nanohardness. *Acta Mater* **59**(20): 7480–7487 (2011)

[32] Bao Y W, Wang W, Zhou Y C. Investigation of the relationship between elastic modulus and hardness based on depth-sensing indentation measurements. *Acta Mater* **52**(18): 5397–5404 (2004)

[33] Musil J. Flexible hard nanocomposite coatings. *RSC Adv* **5**(74): 60482–60495 (2015)

[34] Musil J. Hard nanocomposite coatings: Thermal stability, oxidation resistance and toughness. *Surf Coat Tech* **207**: 50–65 (2012)

[35] Yu C, Yang R, Feng Y H, Huan Y, Peng G J, Zhang T H. Relationships between the work recovery ratio of indentation and plastic parameters for instrumented spherical indentation. *MRS Commun* **5**(1): 89–94 (2015)

[36] Leyland A, Matthews A. On the significance of the *H/E* ratio in wear control: A nanocomposite coating approach to optimised tribological behaviour. *Wear* **246**(1–2): 1–11 (2000)

[37] Pintaude G. Introduction of the ratio of the hardness to the reduced elastic modulus for abrasion. In: *Tribology—Fundamentals and Advancements*. Gegner J, Ed. London, UK: IntechOpen, 2013: 217–230.

Zhen-Yu ZHOU. He received his bachelor's degree in mechanical engineering in 2016 from Zhejiang University of Technology, China. After then, he was a Ph.D. student in Key Laboratory of Special Purpose Equipment and Advanced Processing Technology, Zhejiang University of Technology, China. He has recently obtained his Ph.D. degree in mechanical engineering at Zhejiang University of Technology, China, and subsequently worked as a postdoctoral fellow at Zhejiang University of Technology, China. His research interests include surface engineering and tribology.

Zhong-Yu PIAO. He received his Ph.D. degree in mechanical design and theory from Yanshan University, China. He joined Key Laboratory of Special Purpose Equipment and Advanced Processing Technology, Zhejiang University of Technology, China, from 2012. Now he is a professor of College of Mechanical Engineering, Zhejiang University of Technology, China. His research interests include tribology, surface engineering, state perception, and intelligent manufacturing technology.